Section 4

Parameterization of important atmospheric and surface processes, effects of different parameterizations

Numerical Simulation of Heavy Snowfall and the Potential Role of Ice Nuclei in Cloud Formation and Precipitation Development

Kentaro Araki and Masataka Murakami

Meteorological Research Institute, Tsukuba, Japan
e-mail: araki@mri-jma.go.jp

1. Introduction

A heavy snowfall event occurred in the Kanto region from 14 to 15 February 2014, when a winter extratropical cyclone rapidly developed along the south coast of Japan. The snow depth exceeded the historical record in the region, and the event caused many losses of human life. Accurate forecast of such heavy snowfall events is highly required but remains challenging because the precipitation system deeply involves complicated processes of synoptic- and meso-scale dynamics, boundary layer, cloud microphysics, and diabatic process due to phase changes of cloud and precipitation particles. In terms of cloud microphysics, understanding of the aerosol indirect effect by ice nuclei is required. In order to examine the characteristics of cloud microphysics and potential role of ice nuclei in cloud formation and precipitation development during the event, we performed numerical experiments with a horizontal grid spacing of 1.5 km using the Japan Meteorological Agency (JMA) non-hydrostatic model (NHM; Saito et al. 2006) with bulk cloud microphysics scheme. The initial and boundary conditions were provided from 3-hourly JMA mesoscale analysis and the model domain covered the central part of Japan Island, including the Kanto region. The model was run for 33 hours from 0300 Japan Standard Time (JST; JST = UTC + 9 h) on 14 February 2014.
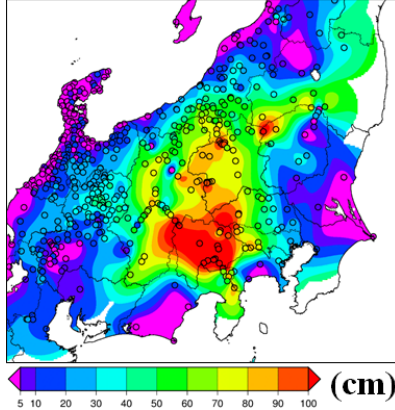

Figure 1. Horizontal distribution of 33-hour accumulated snowfall (cm) from 0300 JST on 14 Febr to 1200 JST on 15 Febr obtained from the sum of the differences of 1-hourly snow depth observations.
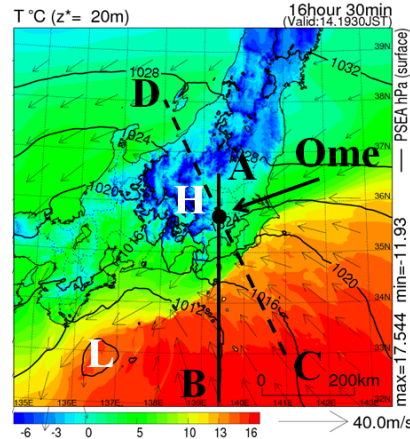

Figure 2. Horizontal distribution of simulated temperature (shade) and sea level pressure (contour) converted from pressure at 20 m above the surface at 1930 JST on 14 Febr. Vectors indicate horizontal wind at the same level.
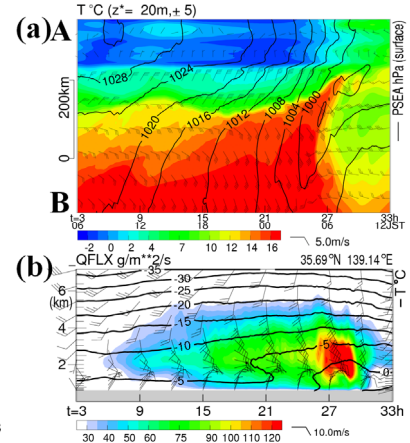

Figure 3. (a) Time-range cross section of simulated temperature at 20 m above the surface (shade) and sea level pressure (contour) along the solid line AB in Fig. 2. (b) Time-height cross section of water vapor flux (shade) and temperature (contour) at the Ome city. Barbs indicate horizontal wind.

2. Microphysical structures in precipitating clouds and the impact of ice nuclei

The snow depth observations provided by many national organizations and local governments revealed the detailed distribution of snow depth, where the 33-hour accumulated snowfall exceeded 1 m in the mountain areas (Fig. 1). The control experiment successfully reproduced the distribution of snowfall (Fig. 4). By comparisons with the surface observation, wind profiler, and liquid water path retrieved from ground-based microwave radiometer data in these regions, simulated dynamic and thermodynamic environment and cloud microphysical properties reasonably agreed with observations (not shown). A coastal front was formed in the south of the Kanto region, and the feature of the cold air damming as U-shaped contour of sea level pressure was found in the Kanto region (Fig. 2). The coastal front got distinct as the north-south gradient of sea level pressure increased (Fig. 3a), and diabatic cooling by sublimation/evaporation/melting of precipitation particles in lower troposphere also contributed to the formation and maintenance of coastal front and cold air damming. A distinct meso-scale vortex, usually called *zipper low*, was formed on the front before the passage of the cyclone (Fig. 2), and would play a role in the maintenance of the coastal front. Warm and moist southeasterly wind flowed on the front, and brought a large amount of water vapor (Fig. 3b), resulting in the heavy snowfall in the Kanto region. The synoptic-scale features of upper-level coupled jet structure, causing acceleration of low-level ageostrophic flows and enhancement of the coastal front, were also found by JMA mesoscale analysis (not shown), which was quite similar to the situation of heavy snowfall events in the east coast of the United States (Uccellini and Kocin 1987).

Clouds composed of solid cloud and precipitation particles were simulated in the 8–12 and 2–4 km layers, and the latter cloud layers were formed both above the surface of the coastal front and on the windward side of the mountains (Fig. 5). Number density of snow was large at a layer between 5 and 10 km altitude and another layer

between 2 and 4 km altitude, and mixing ratio of snow was large below about 8 km altitude. In this case, there were two layers of stratiform ice clouds to the north of the coastal front and on the windward side of the mountains, and the other low-level clouds were also formed by orographically-induced updraft in the mountain regions, resulting in the seeder-feeder mechanism which contributed to the increase of snowfall amount (Houze 2012). On the other hand, the 33-hour accumulated precipitation by graupel reached 20 mm in some parts of the Kanto region (Fig. 4), which was formed by riming growth during the passage of the cyclone over the Kanto plain, where sufficient water vapor supply and super-cooled cloud water locally existed near the center of the cyclone in low-level troposphere.

In order to investigate the effect of ice nuclei (number of cloud ice) on cloud formation and precipitation development, sensitivity experiments were performed by changing coefficients in the formulas of deposition/condensation-freezing-mode ice nucleation (Meyers 1992) and immersion-freezing-mode ice nucleation (Bigg 1955) by factors of 0.1 (IN01) and 10 (IN10). As a result, there were differences of accumulated snow precipitation by of –5 mm in water equivalent for IN01 case and +5 mm for IN10 case as compared with INdef case on the windward side of mountain regions. On the leeward side of mountain regions, there were opposite differences of accumulated precipitation by snow of +5 mm for IN01 and –10 mm for IN10. The accumulated rainfall increased more than 15 mm for IN01 and decreased more than 20 mm for IN10 on the coastal region, whereas the similar amount of rainfall decrease/increase was found off shore. Since there were sufficient water vapor supply below about 6 km altitude (Fig. 3b) and rather low number concentrations of snow for INdef, the conversion of cloud ice into snow and consequent snowfall amount decreased in IN01 and increased in IN10, respectively (Fig. 5). For IN10 case, large number of cloud ice were converted into snow on the windward side of the coastal front over the ocean, and amount of rain produced from melted snow particles increased off shore and decreased on shore and vice versa for IN01 case. The similar contrast was produced on the windward and leeward of low-level orographic clouds; the increase and decrease of snowfall amount on the leeward side of mountains in IN01 and IN10, respectively. This contrast of low-level orographic clouds would be caused by the differences of water vapor supply which increased in IN01 and decreased in IN10 on the windward side of mountains, respectively. On the other hand, precipitation amount by graupel decreased by about 5 mm for IN01 case and increased by more than 10 mm for IN10 case in a part of the Kanto region during the passage of the cyclone. Since there were a large amount of low-level water vapor and supercooled cloud water fluxes as compared with number concentration of snow for INdef case, the increase in snow number concentrations due to enhanced ice nucleation may lead to the increase in graupel precipitation.

3. Conclusions and remarks

The synoptic, mesoscale, and cloud microphysical factors causing a heavy snowfall were investigated through a case study. It's found that the maintenance of the coastal front and the seeder-feeder mechanism were important in the increase of snowfall amount. The result also suggests that concentrations of ice nuclei (cloud ice) considerably affect snowfall amount and its distribution. It's required to develop a numerical model which properly handles the aerosol effects on the cloud formation and precipitation development.
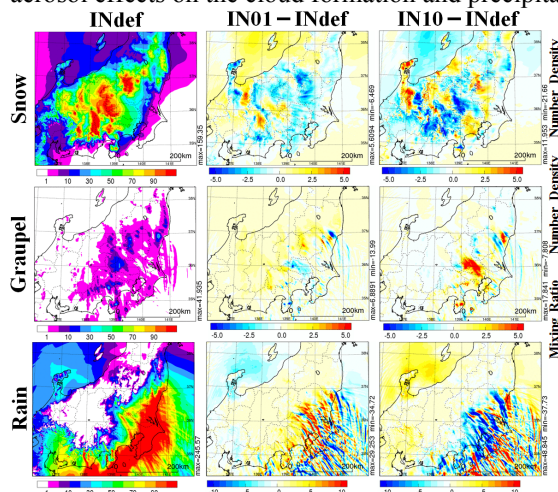

Figure 4. Horizontal distributions of 33-hour accumulated precipitation (mm) from 0300 JST on 14 to 1200 JST on 15 by snow, graupel, and rain simulated by INdef (left panels). Horizontal distributions of the difference between IN01/IN10 and INdef (center/right panels).
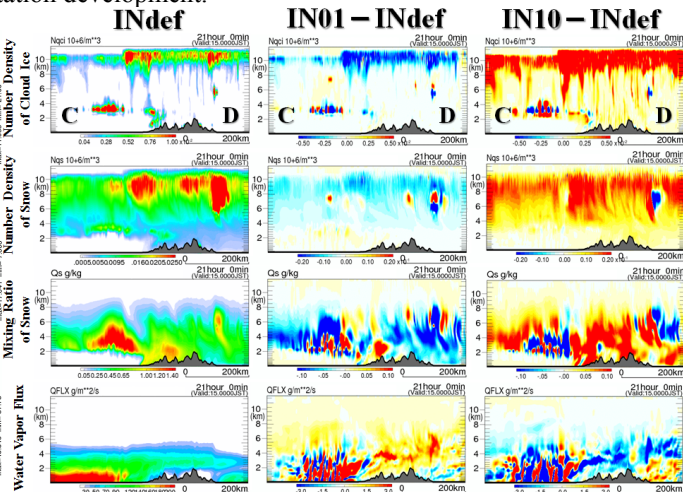
Figure 5. Vertical cross sections of number densities of cloud ice and snow, mixing ratio of snow, and water vapor flux along the broken line CD in Fig. 2 at 0000 JST on 15.

References:

Houze, R. A., 2012: Orographic effects on precipitating clouds. *Rev. Geophys.*, **50**, RG1001, doi:10.1029/2011RG000365.

Saito, K., T. Fujita, Y. Yamada, J. Ishida, Y. Kumagai, K. Aranami, S. Ohmori, R. Nagasawa, S. Kumagai, C. Muroi, T. Kato, H. Eito, and Y. Yamazaki, 2006: The operational JMA nonhydrostatic mesoscale model. *Mon. Wea. Rev.*, **134**, 1266–1298.

Uccellini, L. W., and P. J. Kocin, 1987: The interaction of jet streak circulations during heavy snow events along the east coast of the United States. *Wea. Forecasting*, **2**, 289–308.

Improvement of cumulus convection and planetary boundary layer parameterizations in the NCEP GFS

Jongil Han

NOAA/NWS/NCEP Environmental Modeling Center, College Park, MD, USA,

e-mail: Jongil.Han@noaa.gov

A new shallow cumulus convection scheme has been implemented into the NCEP Global Forecast System (GFS; 2010), which employs a mass flux parameterization replacing the old turbulent diffusion-based approach and helps not to destroy stratocumulus clouds off the West coasts of South America and Africa as the old scheme does. The deep cumulus convection scheme was revised to make cumulus convection stronger and deeper to deplete more instability in the atmospheric column and result in the suppression of the excessive grid-scale precipitation (2010). The planetary boundary layer (PBL) scheme was revised to enhance turbulence diffusion in stratocumulus regions (2010), which helps prevent too much low cloud from forming.

Recently, a hybrid eddy-diffusivity mass-flux (EDMF) PBL scheme with dissipative heating and modified stable PBL mixing has been implemented into the NCEP GFS (2015). With the EDMF PBL scheme, where the nonlocal transport by large turbulent eddies is represented by a mass-flux (MF) scheme and the local transport by small eddies is represented by an eddy-diffusivity (ED) scheme, the daytime PBL growth was improved. In order not to degrade the forecast skill in the tropical ocean where strongly unstable PBLs are rarely found, a hybrid EDMF PBL scheme has been adopted, where the EDMF scheme is applied only for the strongly unstable PBL, while the old GFS eddy-diffusivity counter-gradient (EDCG) scheme is used for the weakly unstable PBL. For the vertical momentum mixing, the MF scheme is modified to include the effect of the updraft-induced pressure gradient force. To enhance a too weak vertical turbulent mixing for weakly and moderately stable conditions, the current local scheme in the stable boundary layer is modified to use an ED profile method. On the other hand, the drag coefficient over sea was reduced in high wind speeds to increase hurricane intensity which is generally weaker than the observation in the GFS due to coarse resolution.

Necessity of parameterizations for convective initiation in high resolution cloud-permitting models

Tabito Hara

Numerical Prediction Division, Japan Meteorological Agency
1-3-4, Ote-machi, Chiyoda-ku, Tokyo 100-8122, Japan

1 Introduction

NWP centers around the world, including the Japan Meteorological Agency (JMA), have recently begun operating high resolution cloud-permitting models with horizontal grid spacing of around 2-km with no convective parameterizations. JMA's operational 2-km model, called the Local Forecast Model (LFM), has been in operation since August 2012, with the forecast domain expanded in May 2013 to cover Japan and the surrounding area. Its initial conditions are generated by three-hour data assimilation cycles combined with the three-dimensional variational assimilation method and one-hour forecasts from the forecasting model. Forecasts are updated every hour.

Higher resolution models are considered capable of resolving a significant part of vertical transportation of momentum, heat and moisture, which is the main feedback of convection, in the form of vertical advection with grid-mean vertical velocities, meaning that no convective parameterizations are required. However, verification to examine the performance of JMA's 2-km operational model revealed issues related to convection such as delays in convective initiation and excessive intensity of convective activities.

This report first outlines verification of the operational 2-km model with focus on convective initiation, then discusses possible reasons for the delays in convective initiation. Finally, an attempt to resolve the issues and its outcome are described.

2 Delay in convective initiation shown by verification of the operational model

Figure 1 shows a timeseries representation of the number of grids in which precipitation exceeding 1 mm/h is observed (red bars) and predicted by the operational model (purple line). The numbers of events are accumulated over several cases in which showers associated with unstably stratified layers occurred. The figure shows that while most events with precipitation exceeding 1 mm/h were observed at 16 JST (Japanese local time), the peak time of current operational predictions delayed by around two hours from the corresponding observation, which means that convection is not initiated at an appropriate time in the current 2-km operational model. Similar tendencies can be also seen in Figure 2 timeseries representation showing the observed and predicted frequencies of precipitation exceeding 10 mm/h.

3 Effects of enhancing the dynamical and boundary layer scheme

JMA replaced the old non-hydrostatic model (JMA-NHM; Saito et al. (2007)) with a new one called "ASUCA" at the end of January 2015 (Aranami et al. 2015). ASUCA has been developed as a new dynamical core with higher accuracy and better computational efficiency on massive parallel scalar supercomputers. Physical processes equivalent to or more enhanced than those of the JMA-NHM were implemented via use of the "Physics library" (Hara et al. 2012). In particular, the improved Mellor-Yamada-Nakanishi-Niino level 3 model (MYNN3; Nakanishi and Niino (2009)) used as a boundary layer turbulence scheme was refined so that turbulent fluxes and tendencies of prognostic variables in the turbulence scheme can be stably solved, removing temporarily fluctuated, noisy, and overestimated turbulent fluxes.

In the initial stage of ASUCA development, no convective parameterization was implemented (as with the operational model employing JMA-NHM at the time). For the delay in convective initiation described in the previous section, ASUCA improved the delay in precipitation peak as shown by the green line in Figure 1 (although the frequency shortage at the initiation stage remains unresolved). This implies that refinement of the dynamical and the boundary layer scheme is highly related to the timing of convective initiation. However, the delay still has room for improvement.

4 Possible cause of convective initiation delay

It is considered that the main feedback of convection such as vertical transport of momentum, heat and moisture can be represented by grid-mean vertical velocity in models with a horizontal resolution of a few kilometers or less. However, this does not necessarily mean that all phenomena (especially initiating and controlling convection) can be resolved in high resolution models. For example, the forced lifting necessary to initiate convection would often be induced by small scale convergence and small scale topography variance, but some cases may not be resolved even if vertical transport is represented. The lack of smaller phenomena related to convective initiation in the models explains the delay in convective precipitation peaks predicted by the 2-km operational model and even the newer model in comparison with observations.

5 Parameterization for convective initiation

As an attempt, a parameterization to represent convective initiation was implemented in ASUCA. The parameterization is based on the existing convective parameterization suggested by Kain and Fritsch (1990) (known as KF scheme), but it has been modified assuming slower convective stabilization, implying that tendency from convective processes is much smaller than for the original convective parameterization.

The KF convection scheme, which is employed in the 5-km operational meso scale model at JMA, diagnoses a final state in which a certain ratio r of the initial convective available potential energy (CAPE) is removed for a certain life time of convection τ:

$$\frac{d\text{CAPE}}{dt} = -(1-r)\frac{\text{CAPE}_{\text{initial}}}{\tau}. \quad (1)$$

Tendencies of prognostic variables ϕ are calculated using the difference between the initial and final states
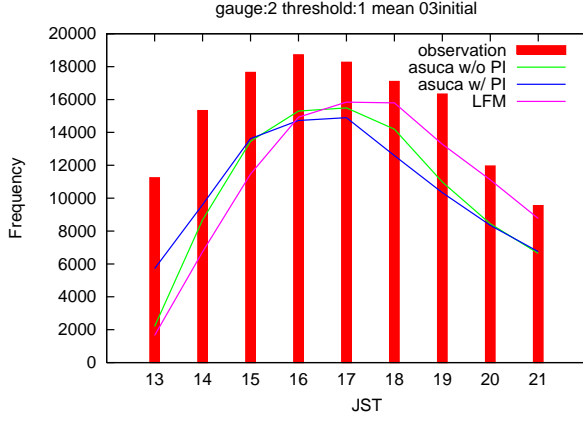
Fig. 1: Timeseries representation of the number of grids at which precipitation exceeding 1 mm/h is observed (red bars) and predicted by models (lines). Purple line: the operational model, green and blue lines: ASUCA without / with the parameterization of initiation, respectively
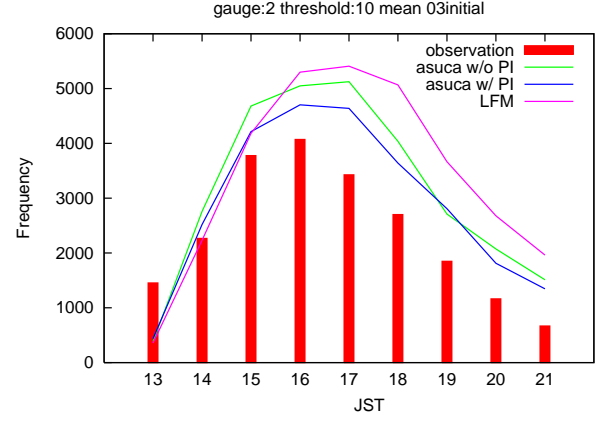

Fig. 2: As per Figure 1, but for precipitation exceeding 10mm/h

(ϕ_{initial} and ϕ_{final}, respectively) :

$$\frac{\partial \phi}{\partial t} = \frac{\phi_{\text{final}} - \phi_{\text{initial}}}{\tau}. \qquad (2)$$

In the modified scheme to parameterize convective initiation, a longer value of τ is adopted (meaning weaker convective activity and smaller tendencies from convection) aiming at representing weaker vertical transport and release of latent heat in the initial stage of convection. In addition, the convection scheme is modified so that final states and tendencies are diagnosed at every timestep, as opposed to the fixed-interval evaluation of the original KF scheme (e.g. five minutes). Updating of tendencies at every timestep makes the modified scheme more sensitive to developing convection produced by dynamical processes in models.

If dynamical processes in models do not produce updraft due to convection even with the realization of an unstably stratified layer, the parameterization is activated and modifies layer stratification by weakly transporting heat and moisture vertically and releasing latent heat through the phase transition of water, resulting in the production of a local low pressure area. Once such a local low pressure area is generated, dynamical processes in models calculate convergence into the low pressure area and promotes development of convection. As it acts very weakly, the parameterization just helps dynamical processes to foster the convective system.

The blue lines in Figures 1 and 2 indicate forecast frequency from ASUCA with the parameterization to help initiation. For levels of precipitation exceeding 1 mm/h (Figure 1), the forecast frequency at 13 JST (usually the initial stage of convection) is much closer to the observation frequency (but still smaller than the actual observation). The overall temporal evolution of precipitation frequency is also significantly improved for precipitation exceeding both 1 mm/h and 10 mm/h (Figure 2). The new parameterization is proven to be quite effective in easing convective initiation delay.

6 Discussion

Development of the proposed parameterization for convective initiation was motivated by recognition that various scales related to convective phenomena are mixed.

While the parameterization currently targets convective initiation which cannot necessarily be resolved even in cloud-permitting models with horizontal grid spacing of a few kilometers, there are other phenomena that cannot be resolved even if vertical transport by convection is represented. By way of example, entrainment plays an important role because it controls convective activity by diluting cumuli. However, its scale may be too small to resolve in cloud-permitting models. This may be one reason why overly strong vertical velocity is sometimes predicted in high resolution models when no convective schemes are adopted. To represent the effect of entrainment-related weakening of convective activity (and secure computational stability) in ASUCA, vertical velocity is suppressed by adding an extra term to its tendency. However, evaluation of this extra term has no robust physical basis because it depends only on the CFL conditions and involves no consideration for the physical processes of entrainment. More physical methods of estimating effects of entrainment are necessary for further model improvement.

The proposed parameterization for convective initiation is just one example, and it is challenging to treat resolved and unresolved phenomena at the same time. It is exactly related to "Grey Zone" problem.

References

Aranami, K., T. Hara, Y. Ikuta, K. Kawano, K. Matsubayashi, H. Kusabiraki, T. Ito, T. Egawa, K. Yamashita, Y. Ota, Y. Ishikawa, T. Fujita, and J. Ishida, 2015: A new operational regional model for convection-permitting numerical weather prediction at JMA. *CAS/JSC WGNE Res. Activ. Atmos. Oceanic Modell.*, **45**, submitted.

Hara, T., K. Kawano, K. Aranami, Y. Kitamura, M. Sakamoto, H. Kusabiraki, C. Muroi, and J. Ishida, 2012: Development of the Physics Library and its application to ASUCA. *CAS/JSC WGNE Res. Activ. Atmos. Oceanic Modell.*, **42**, 0505–0506.

Kain, J. S. and J. M. Fritsch, 1990: A One-Dimensional Entraining/Detraining Plume Model and Its Application in Convective Parameterization. *J. Atmos. Sci.*, **47**, 2784–2802.

Nakanishi, M. and H. Niino, 2009: Development of an Improved Turbulence Closure Model for the Atmospheric Boundary Layer. *J. Meteor. Soc. Japan*, **87**, 895–912.

Saito, K., J. Ishida, K. Aranami, T. Hara, T. Segawa, M. Narita, and Y. Honda, 2007: Nonhydrostatic Atmospheric Models and Operational Development at JMA. *J. Meteor. Soc. Japan*, **85B**, 271–304.

Factors of model underestimation of snow fall over the Japan-Sea coastal areas in middle Japan: Comparison with observed precipitation particles

Teruyuki Kato[1], Hiroki Motoyoshi[2], Yoshinori Yamada[1], Akihiko Hashimoto[1], Sento Nakai[2], Masaaki Ishizaka[2]

[1]Meteorological Research Institute/Japan Meteorological Agency (Email: tkato@mri-jma.go.jp)
[2]Snow and Ice Research Center/National Research Institute for Earth Science and Disaster Prevention

1. Introduction

Polar air outbreak from the Eurasia Continent often brings heavy snow fall over the Japan-Sea coastal areas during the winter season. The Japan Meteorological Agency (JMA) operational mesoscale model (horizontal resolution: 5 km), however, usually underestimates snow fall amounts over plain areas, while mountainous areas have overestimations. In Snow and Ice Research Center of National Research Institute for Earth Science and Disaster Prevention, located in the plain area (see the location marked by symbol of X in Fig. 2), the size and terminal velocity of precipitation particles have been captured every minute by a charge-coupled device camera and a Parsivel optical disdrometer. Then by using the method of Ishizaka et al. (2013), the main type of solid hydrometeors contributing to precipitation has been identified from the relationship between measured size and fall speed every five minutes (e.g., see Fig. 1a).

In this study, hydrometeor types simulated by JMA nonhydrostatic model (NHM: Saito et al. 2007) with difference resolution are compared with identified observation ones, and the underestimation of snowfall amounts over plain areas is examined.
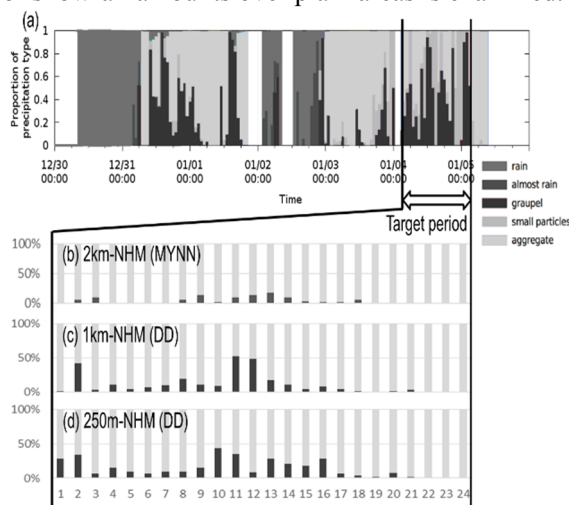

Fig. 1 (a) Identified observation types of hydrometeors between 30 November 2012 and 05 January 2013. Same as (a), but results simulated by (b) 2km, (c) 1km and (d) 250m models during one day from 03 JST January 2013.

2. Experimental designs

One-day forecasts from 03 JST (=UTC+ 9hs) 04 January 2013 were conducted using initial and boundary conditions produced from 3-hourly available JMA mesoscale analyses with a horizontal resolution of 5 km. At first a 5km-NHM with a large domain (2500x 2000km) was run, and then for a small domain of 850x550km 2km and 1km-NHMs were run nested within 5km-NHM forecasts. Further, for a domain of 330x250km 500m and 250m-NHMs were run nested within forecasts of 1km-NHM. A bulk-type microphysics parameterization scheme in which two moments are treated only for ice hydrometeors is used for precipitation processes, and the Kain-Fritsch convection parameterization scheme is additionally used only in 5km-NHM. The turbulence closure scheme of Mellor-Yamada-Nakanishi-Niino level-3 (MYNN: Nakanishi and Niino 2006) is used in 5km, 2km, and 1km-NHMs, while Deardroff (DD) scheme (1980) is used in 1km, 500m and 250m-NHMs.

3. Comparison with observations

The underestimation of snow fall amounts including graupel over plain areas indicated by ellipses in Figs. 2a and 2b is improved using 1km-NHM (Fig. 2d). This improvement is mainly caused by the production of graupel around coastal areas (Fig. 2c), while 5km-NHM hardly produces graupel (not shown) and graupel ratios of 2km-NHM (Fig. 2b) are less 50% of those of 1km-NHM (Fig. 1c). The proportion of graupel in 1km-NHM, however, is considerably smaller in comparison with identified observation types of hydrometeors (Fig. 1a). This small ratio is not improved using 250m-NHM (Fig. 1d). These improvements and resolution dependency agree with Kato (2011, 2012).

4. Effect of terminal velocity

In 5km-NHM, instead of graupel, snow particles could be excessively produced and most of them move to mountainous areas without falling down due to the terrain-induced upward motion (Fig. 3a).

To ascertain this hypothesis, a sensitivity experiment in which the terminal velocity of snow on land is replaced with that of graupel was conducted using 5km-NHM. The results (Figs. 2c and 3b) show the improvement of underestimation of snow fall amounts over plain areas, and that of excessively production of snow particles, which suggests that a new parameterization of the production of graupel is necessary for coarse resolution models.

5. Other Impacts on snowfall amounts

Much water cloud is necessary for the production of graupel (i.e. riming process). Since cloud ice hardly exists in warm-rain clouds with the temperature higher than -4°C, cloud ice crystal nucleating activity is restricted above -4°C to increase cloud water amounts. The results of 2km- and 1km-NHMs, however, showed no improvement for the production of graupel. Another sensitivity experiment in which the evaporation of graupel is restricted also hardly impacts the graupel fall amounts on the ground, because low-level humidity around coastal areas is high (~80%). On the other hand, the restriction of the evaporation of snow causes the increase of snowfall amounts over the sea and the decrease over plain areas, which agrees with Kato (2011).
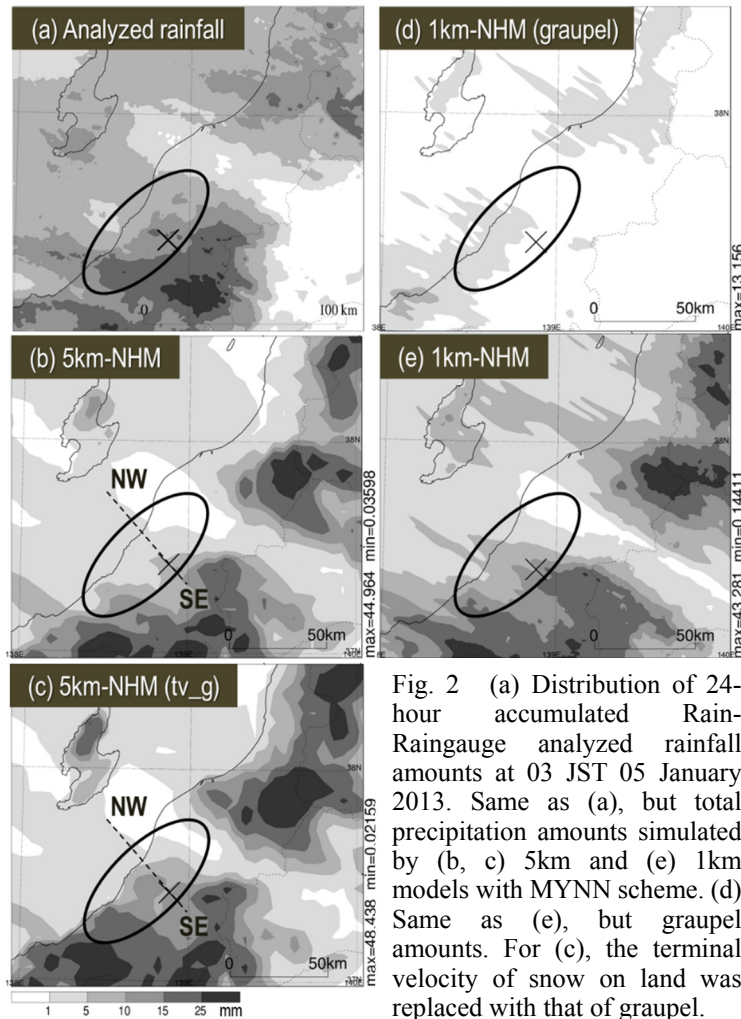

Fig. 2 (a) Distribution of 24-hour accumulated Rain-Raingauge analyzed rainfall amounts at 03 JST 05 January 2013. Same as (a), but total precipitation amounts simulated by (b, c) 5km and (e) 1km models with MYNN scheme. (d) Same as (e), but graupel amounts. For (c), the terminal velocity of snow on land was replaced with that of graupel.

References

Ishizaka, M., H. Motoyoshi, S. Nakai, T. Shiina, T. Kumakura, and K. Muramoto, 2013: *J. Meteor. Soc. Japan*, **91**, 747-762.

Kato, T., 2012: CAS/JSC Research Activities in Atmospheric and Oceanic Modeling, **42**, 4.09-4.10.

Kato, T., 2011: CAS/JSC Research Activities in Atmospheric and Oceanic Modeling, **41**, 3.03-3.04.

Saito, K., J. Ishida, K. Aranami, T. Hara, T. Segawa, M. Nareta, and Y. Honda, 2007: *J. Meteor. Soc. Japan*, **85B**, 271-304.
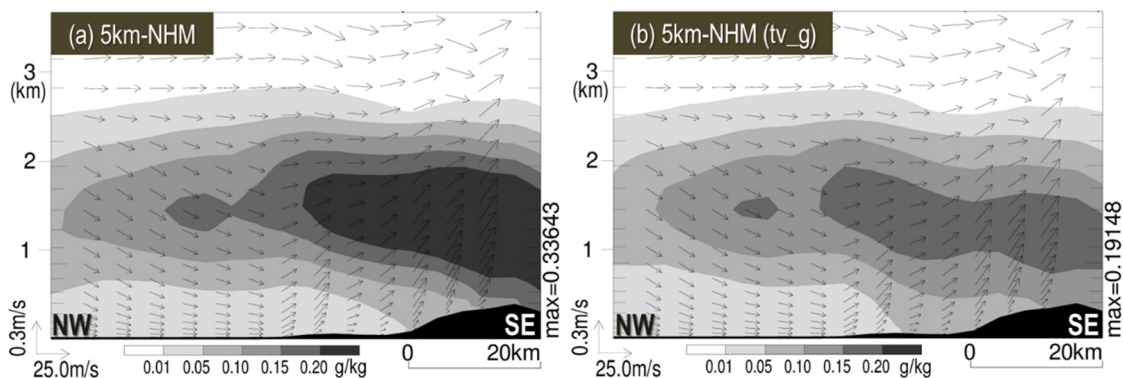
Fig. 3 (a) Vertical cross section of 24-hour mean snow mixing ratios on the dashed line in Fig. 2b, simulated by 5km-NHM. Wind vectors show streams projected on the section. (b) Same as (a), but the terminal velocity of snow on land was replaced with that of graupel.

Inner Time Loop Application for Vertical Turbulent Diffusion Processes

Takuya KOMORI

Climate Prediction Division, Japan Meteorological Agency, Tokyo, Japan
Email: komori@met.kishou.go.jp

1. INTRODUCTION

In operational numerical prediction models, efforts have been made to use a longer time-step as a way of reducing the computational cost. However, detailed investigation of the Global Spectral Model (GSM) in an idealized experiment revealed that numerical instability could be occurred in tendencies due to vertical turbulent diffusion with the over-implicit scheme in certain situations over land, where surface turbulent fluxes increased rapidly after sunrise and became large. These results suggest that a shorter time-step should potentially be used in the operational system (JMA 2013). Accordingly, an inner time loop was applied in the GSM for the calculation of vertical turbulent diffusion processes with a shorter time-step to alleviate numerical instability. This reduces the computational cost in operational use as compared to that incurred in the application of a shorter time-step for all processes in the model.

2. INNER TIME LOOP APPLICATION

Using an inner time loop, processes can be calculated with a shorter time-step, $\Delta t'$, than the normal time-step, Δt, depending on the number of the time loops N : $\Delta t' = \Delta t / N$. Accordingly, doubling N will halve the time-step in a process. In this study, an inner time loop was introduced after calculation of fluxes and tendencies due to short and long waves, thereby enabling skin temperature updating before calling of the vertical turbulent diffusion scheme (VDF). To maintain interaction between the lowest model level and the surface via vertical turbulent transport at each inner time-step, calculation of surface turbulent fluxes (SURF) was also included in the inner time loop. The tendencies of the forecast variable ϕ_N in each inner time loop were added to update the variable in the previous loop ϕ_{N-1}, where ϕ_1 is identical to the forecast variable ϕ, in the normal time-step. All estimated tendencies in the inner time loops were summed up and added to tendencies due to radiation (RAD), convection (CONV), cloud (CLD), and both orographic and non-orographic gravity wave drags (GWD) as part of physics processes (PHY) at every normal time-step as follows:

$$\left(\frac{\partial \phi}{\partial t}\right)_{PHY} = \left(\frac{\partial \phi}{\partial t}\right)_{RAD} + \left(\frac{\partial \phi}{\partial t}\right)_{CONV} + \left(\frac{\partial \phi}{\partial t}\right)_{CLD} + \left(\frac{\partial \phi}{\partial t}\right)_{GWD} + \frac{1}{N}\sum_{1}^{N}\left(\frac{\partial \phi_N}{\partial t'}\right)_{VDF+SURF}$$

3. EVALUATION

Two experiments (CNTL and TEST) were conducted to evaluate the impact of the inner time loop in 84-hour forecasts. The CNTL experiment was based on the GSM. In the TEST experiment, an inner time loop with a halved time-step (N = 2) was applied to vertical turbulent diffusion and surface processes. Figures 1 and 2 respectively show the simulated temperature and moisture tendencies due to physical processes in pressure-time cross sections at the ARM (Atmospheric Radiation Measurement) SGP (Southern Great Plains) site. As a general characteristic, no significant difference was seen between CNTL and TEST around the site. The model-level output in CNTL at each time-step up to the 84-hour forecast with an initial time of 00 UTC on 4 August 2013 exhibited numerical oscillation with changes in the tendency of the positive/negative characteristic in turn with each time step in certain situations. Conversely, no numerical oscillation was observed in TEST, which was characterized by smoothed and increased tendencies. Performance was verified against wind-profiler observation data distributed via WMO's global telecommunication system from near the ARM SGP site. Figure 3 shows pressure-time cross sections of wind speeds as simulated in the CNTL and TEST experiments, as well as wind-profiler observation data. During this period, the nocturnal low level jet (NLLJ) was observed over the Great Plains every night. The wind speeds in TEST were enhanced in association with the potential temperature profiles with decoupling of the nocturnal stable boundary layer (not shown). This makes the NLLJ representation closer to the observation in comparison with CNTL, though there is still room for improvement. Accordingly, as well has helping to alleviate instability, the results of this study also represent a useful step toward better atmospheric representation. Further investigation is needed to explore the sensitivity of land-atmosphere coupling.

REFERENCE

JMA, 2013: Outline of the operational numerical weather prediction at the Japan Meteorological Agency. Appendix to WMO technical progress report on the global data-processing and forecasting system and numerical weather prediction research. 188pp. Available online:
http://www.jma.go.jp/jma/jma-eng/jma-center/nwp/outline2013-nwp/index.htm
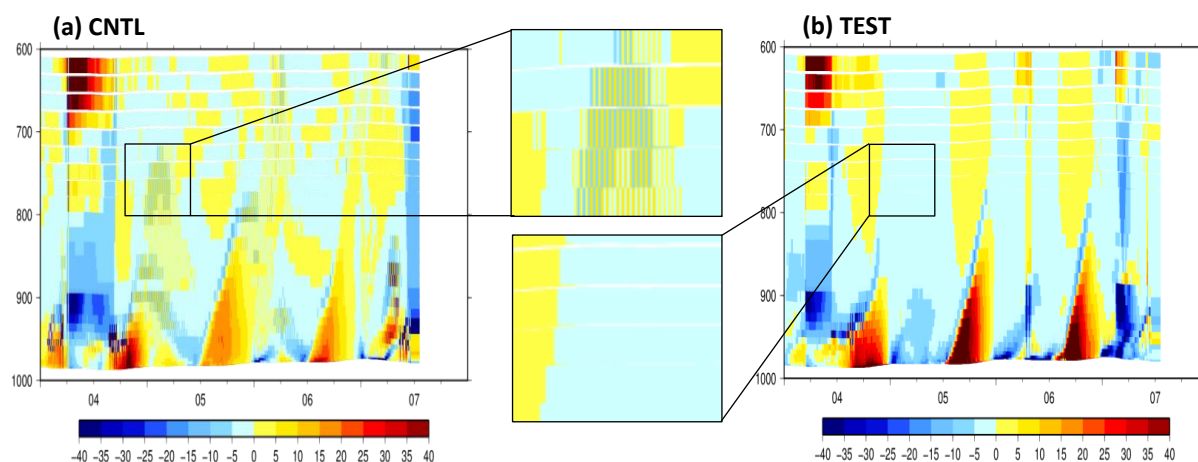
Figure 1. Pressure-time cross section of temperature tendency due to physical processes [K/day] for the (a) CNTL and (b) TEST experiments at the ARM SGP site. Model-level data were output at every time-step up to the 84-hour forecast with an initial time of 00 UTC on 4 August 2013.
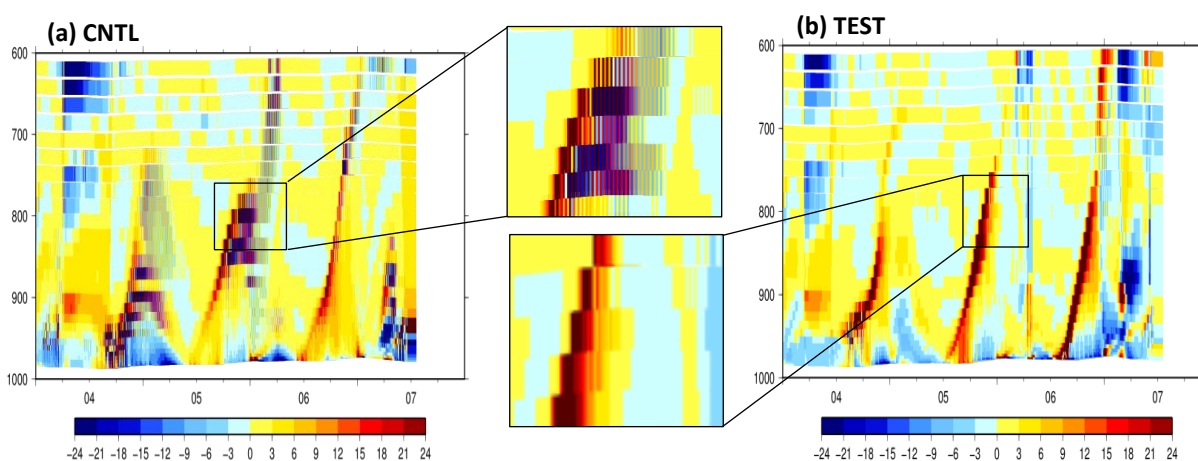

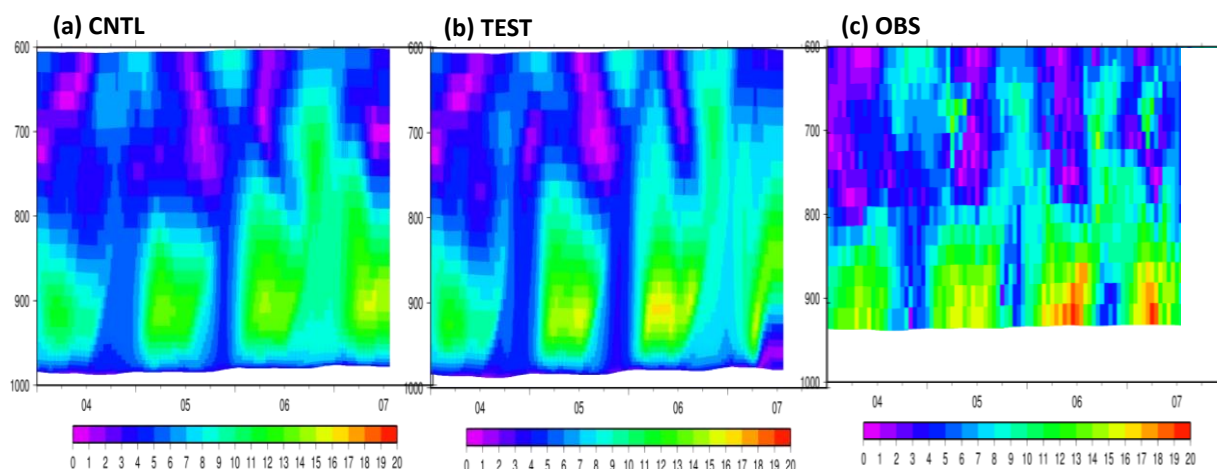Figure 2. Same as Figure 1, but for moisture tendency due to physical processes [g/kg/day].

Figure 3. Pressure-time cross sections of wind speeds [m/s] for the (a) CNTL experiment, (b) TEST experiment and (c) wind-profiler observation near the ARM SGP site. In the experiments, model-level data were output hourly up to the 84-hour forecast with an initial time of 00 UTC on 4 August 2013.

Toward developing global aerosol modeling and data assimilation capabilities at NOAA/NCEP for improving weather and air quality forecasts

Sarah Lu (Sarah.Lu@noaa.gov) and Jun Wang (Jun.Wang@noaa.gov) NOAA/
NWS/NCEP Environmental Modeling Center, College Park, MD, USA

NCEP recently implemented the NEMS GFS Aerosol Component (NGAC) for global dust forecasts. With further development, NEMS GFS can be used for modeling and assimilating aerosols and reactive gases on a global scale. The global modeling/assimilation efforts not only allow aerosol impacts on weather forecasts and climate predictions to be considered, but also enable NCEP to provide quality atmospheric constituent products serving a wide-range of stakeholders, such as health professionals, aviation authorities, policy makers, and solar energy plant managers.

NCEP's global in-line aerosol forecast system

NASA's bulk aerosol scheme (an in-line version of the Goddard Chemistry, Aerosol, Radiation, and Transport model [GOCART], Chin et al., 2002; Colarco et al., 2010) has been incorporated into the NOAA Environmental Modeling System (NEMS) to establish the first interactive global aerosol forecasting system, NEMS GFS Aerosol Component (NGAC), at NCEP (Lu et al., 2013). The NGAC was added to NCEP's production suite in 2012, providing 120-hour daily global dust forecasts. A major NGAC upgrade (multi-species forecasts for dust, sea salt, sulfate, and carbonaceous aerosols using near-real-time satellite-based smoke emissions) is slated for operational implementation in late 2015.

The rationale for developing the global aerosol forecasting capabilities at NOAA includes: (1) to improve weather forecasts and climate predictions by taking into account aerosol effects on radiation and clouds; (2) to provide a first step toward aerosol data assimilation and reanalysis; (3) to improve assimilation of satellite observations by properly accounting for aerosol effects; (4) to provide aerosol (lateral and upper) boundary conditions for regional air quality predictions; and (5) to produce quality aerosol information that addresses societal needs and stakeholder requirements, e.g., UV index, ocean productivity, visibility, air quality, and sea surface temperature retrievals.

Applications of NGAC products

The Consensus International Cooperative for Aerosol Prediction (ICAP) multi-model ensemble (ICAP-MMES, Sessions et al., 2015) became pseudo-operational in 2014, using four complete aerosol forecast models from the European Centre for Medium-Range Forecasts (ECMWF), Naval Research
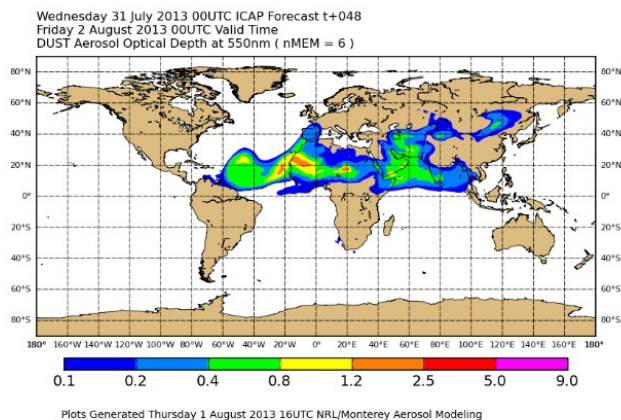
Figure 1 Dust AOD valid at 12 UTC 1st August 2013 for ICAP MMEs (6-members, including NGAC).

Laboratory (NRL), Japan Meteorological Agency (JMA), and NASA Global Modeling and Assimilation Office (GMAO) as well as three dust-only models from NCEP (i.e., NGAC), U.K. Met Office (UKMO), and Barcelona Supercomputing Center (BSC). Figure 1 shows the dust AOD from the ICAP Multi- Model Ensembles (ICAP-MME), valid at 12 UTC 1 August 2013.

Efforts are under way to couple NGAC with NCEP's regional air quality system, which is the Community Multi-Scale Air Quality (CMAQ) model driven by NCEP's North American Mesoscale (NAM) model. Figure 2 shows the observed and modeled surface

fine particulate matter (PM2.5) at Miami. The baseline run uses static LBCs and the experimental run uses dynamic LBCs from NGAC. It is found that the inclusion of long-range dust transport via dynamic LBCs leads to an improvement in CMAQ forecasts during dust intrusion episodes.

Figure 2 PM2.5 at Miami for two CMAQ runs.

Future Directions

As NGAC introduces a prognostic aerosol capability at NCEP, several aerosol-related activities are on-going or planned. These include but are not limited to: (1) extending the aerosol forecast system to include aerosol observations in an effort to initialize the aerosol model; (2) improving the representation of aerosol processes, cloud microphysics, and aerosol-cloud-radiation interaction in NCEP global models; (3) exploring how much complexity is needed to accurately represent the aerosol processes and effectively account for aerosol effects during data assimilation; (4) developing an observation-based diagnosis package to evaluate physically-based aerosol-cloud schemes; (5) providing global aerosol products for various downstream applications, such as using global aerosol fields as LBCs for regional air quality models and linking aerosol forecasts with UV index, sea surface temperature retrievals, and solar electricity production forecasts.
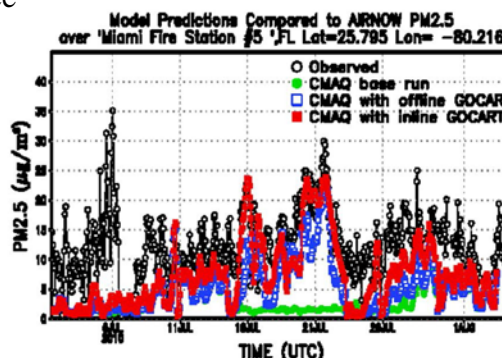
An improved approximation for the moist-air entropy potential temperature θ_s

Pascal Marquet

Météo-France. CNRM/GMAP. Toulouse. France. *E-mail: pascal.marquet@meteo.fr*

1   Motivations

The moist-air entropy is defined in Marquet (2011, hereafter M11) by $\boxed{s = s_{ref} + c_{pd} \ \ln(\theta_s)}$ in terms of two constant values (s_{ref}, c_{pd}) and a potential entropy temperature denoted by θ_s. It is shown in M11 that a quantity denoted by $(\theta_s)_1$ plays the role of a leading order approximation of θ_s.

The aim of this note is to demonstrate in a more rigorous way that $(\theta_s)_1$ is indeed the leading order approximation of θ_s, and to derive a second order approximation which may be used in computations of values, gradients or turbulent fluxes of moist-air entropy. Some impacts of this second order approximation are described in this brief version of a note to be submitted to the QJRMS.

2   Definition of θ_s and $(\theta_s)_1$

The potential temperature θ_s is defined in M11 by

$$\boxed{\theta_s = (\theta_s)_1 \left(\frac{T}{T_r}\right)^{\lambda \, q_t} \left(\frac{p}{p_r}\right)^{-\kappa \, \delta \, q_t} \left(\frac{r_r}{r_v}\right)^{\gamma \, q_t} \frac{(1+\eta \, r_v)^{\kappa \, (1+\delta \, q_t)}}{(1+\eta \, r_r)^{\kappa \, \delta \, q_t}}}$$

$$\text{where} \quad \boxed{(\theta_s)_1 = \theta_l \ \exp(\Lambda_r \, q_t) \ .} \tag{1}$$

This definition of θ_s is rather complex, but the more simple quantity $(\theta_s)_1$ was considered in M11 as a leading order approximation of θ_s, where the Betts' potential temperature is written as $\theta_l = \theta \ \exp[-(L_v \, q_l + L_s \, q_i)/(c_{pd} \, T)]$.

The total water specific content is $q_t = q_v + q_l + q_i$ and r_v is the water vapour mixing ratio. Other thermodynamic constants are: $R_d \approx 287$ J K^{-1}, $R_v \approx 461.5$ J K^{-1}, $c_{pd} \approx 1005$ J K^{-1}, $c_{pv} \approx 1846$ J K^{-1}, $\kappa = R_d/c_{pd} \approx 0.286$, $\lambda = c_{pv}/c_{pd} - 1 \approx 0.838$, $\delta = R_v/R_d - 1 \approx 0.608$, $\eta = R_v/R_d \approx 1.608$, , $\varepsilon = R_d/R_v \approx 0.622$ and $\gamma = R_v/c_{pd} \approx 0.46$.

The term

$$\boxed{\Lambda_r = [\, (s_v)_r - (s_d)_r \,] \ / \ c_{pd} \ \approx \ 5.87} \tag{2}$$

depends on reference entropies of dry air and water vapour at $T_r = 0$ C, denoted by $(s_d)_r = s_d(T_r, e_r)$ and $(s_v)_r = s_v(T_r, p_r - e_r)$, where $e_r = 6.11$ hPa is the saturating pressure at T_r and $p_r = 1000$ hPa. The two reference entropies $(s_v)_r \approx 12673$ J K^{-1} and $(s_d)_r \approx 6777$ J K^{-1} are computed in M11 from the Third Law of thermodynamics, leading to $\Lambda_r \approx 5.87$. The reference mixing ratio is $r_r = \varepsilon \, e_r \, / \, (p_r - e_r) \approx 3.82$ g kg^{-1}.

3   Computations of Λ_s and $\Lambda_\star$

Let us define Λ_s by the formula $\theta_s = \theta_l \ \exp(\Lambda_s \, q_t)$ where θ_s, θ_l and q_t are known quantities, and thus by

$$\Lambda_s = \frac{1}{q_t} \ \ln\left(\frac{\theta_s}{\theta_l}\right). \tag{3}$$

The aim is to compute Λ_s from (3) for a series of 16 vertical profiles of stratocumulus and cumulus with varying values of q_t, θ_s and θ_l, in order to analyse the discrepancy of Λ_s from the constant value $\Lambda_r \approx 5.87$ given by (2).

A trial and error process has shown that plotting Λ_s against $\ln(r_v)$ leads to relevant results (see Fig.1). Clearly, all stratocumulus and cumulus profiles are nearly aligned along a straight line with a slope of about -0.46. It is likely that this slope must correspond to $-\gamma$. This linear law appears to be valid for a large range of r_v (from 0.2 to 24 g kg^{-1}).
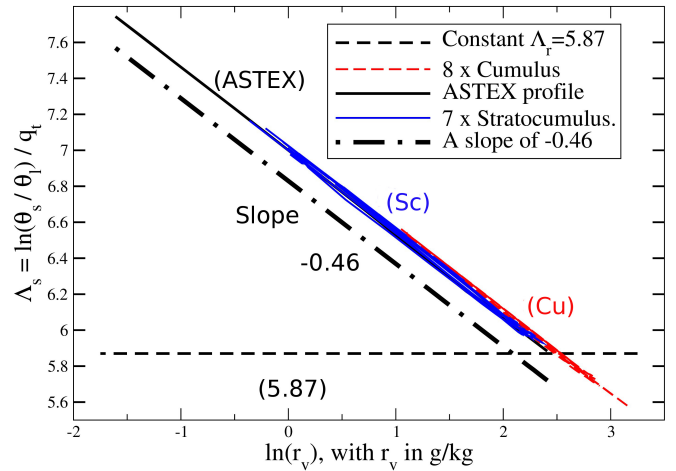

Figure 1: *A plot of Λ_s against $\ln(r_v)$ for 8 cumulus (dashed red), 7 stratocumulus (solid blue) and ASTEX (solid black) vertical profiles. The constant value $\Lambda_r \approx 5.87$ corresponds to the horizontal dashed black line. An arbitrary line with a slope of -0.46 is added in dashed-dotted thick black line*

It is then useful to find a mixing ratio $r_\star$ for which

$$\Lambda_s \approx \Lambda_\star = 5.87 - 0.46 \ \ln(r_v/r_\star) \tag{4}$$

hold true, where $r_\star$ will play the role of positioning the dashed-dotted thick black line of slope $-\gamma \approx -0.46$ in between the cumulus and stratocumulus profiles. This corresponds to a linear fitting of r_v against $\exp[\,(\Lambda_r - \Lambda_s)/\gamma\,]$, $r_\star$ being the average slope of the scattered data points. It is shown in Fig.2 that the value $r_\star \approx 12.4$ g kg^{-1} corresponds to a relevant fitting of all cumulus and stratocumulus vertical profiles for a range of r_v up to 24 g kg^{-1}.
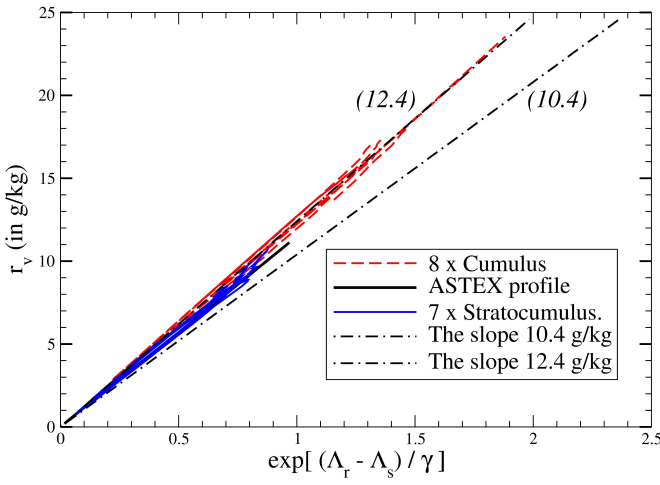
Figure 2: *Same as Fig.1, but with r_v plotted against the quantity $\exp[\,(\Lambda_r - \Lambda_s)/\gamma\,]$. Two lines of slope $r_* = 10.4$ and 12.4 g kg^{-1} are added as dashed-dotted thin black lines.*

It is shown in Fig.3 that Λ_s can indeed be approximated by $\Lambda_\star(r_v, r_*)$ given by (4), with a clear improved accuracy in comparison with the constant value $\Lambda_r \approx 5.87$ for a range of r_v between 0.2 and 24 g kg^{-1}. Curves of $\Lambda_\star(r_v, r_*)$ with $r_* = 10.4$ and 12.4 g kg^{-1} (solid black lines) both simulate with a good accuracy the non-linear variation of Λ_s with r_v, and both simulate the rapid increase of Λ_s for $r_v < 2$ g kg^{-1}.
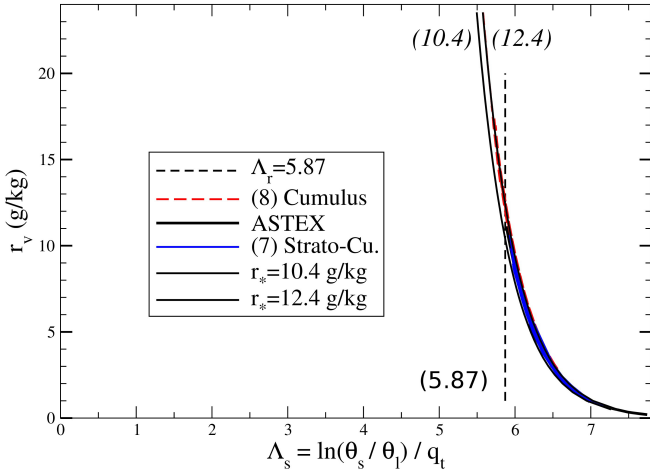

Figure 3: *Same as Fig.1, but with r_v plotted against the quantity Λ_s. The two thin black lines correspond to (4) with $r_* = 10.4$ or 12.4 g kg^{-1}.*

4   Mathematical computation of $\Lambda_\star$

It is important to confirm, by using mathematical arguments, that $(\theta_s)_1$ corresponds to the leading order approximation of θ_s, and that the slope of $-\gamma \approx -0.46$ (with $r_* \approx 10.4$ or 12.4 g kg^{-1}) corresponds to a relevant second order approximation for θ_s. These results are briefly mentioned in Marquet and Geleyn (2015).

First- and second-order approximations of θ_s can be derived by computing Taylor expansions for most of terms in the first formula recalled in Section 2.

The main result is that the term $(r_r/r_v)^{(\gamma\, q_t)}$ is exactly equal to $\exp[\,-(\gamma\, q_t)\,\ln(r_v/r_r)\,]$.

Then, the first order expansion of $(1+\eta\, r_v)^{[\,\kappa\,(1+\delta\, q_t)\,]}$ for small $r_v \approx q_t$ is equal to $\exp(\,\gamma\, q_t)$, since $\gamma = \kappa\,\eta$. The last term $(1+\eta\, r_r)^{(\kappa\,\delta\, q_t)}$ leads to the higher order term $\exp[\,\gamma\,\delta\, q_t\, r_r\,] \approx \exp[\, O(q_t^2)\,]$, since $r_r \ll 1$ and $q_t \ll 1$. Other terms depending on temperature and pressure are exactly equal to $\exp[\,\lambda\, q_t\,\ln(T/T_r)\,]$ and $\exp[\,-\kappa\,\delta\, q_t\,\ln(p/p_r)\,]$.

The Taylor expansion of θ_s can thus be written as

$$\theta_s \approx \theta \, \exp\left(-\frac{L_{\text{vap}}\, q_l + L_{\text{sub}}\, q_i}{c_{pd}\, T}\right) \exp\left(\Lambda_*\, q_t\right) \quad (5)$$

$$\times \exp\left\{q_t\left[\lambda\,\ln\left(\frac{T}{T_r}\right) - \kappa\,\delta\,\ln\left(\frac{p}{p_r}\right)\right] + O(q_t^2)\right\},$$

where $\boxed{\Lambda_* = \Lambda_r \, - \, \gamma\,\ln(r_v/r_*)}$

and $r_* = r_r \times \exp(1) \approx 10.4$ g kg^{-1} (see Figs.2 and 3).

The first order approximation of θ_s is thus given by the first line of (5) with $\Lambda_* = \Lambda_r$, namely by the expected $(\theta_s)_1$. An improved second order approximation is obtained by using Λ_* instead of Λ_r and by taking into account the small corrective term $-\gamma\,\ln(r_v/r_*)$.

Impacts of the second line of (5) with terms depending on temperature and pressure lead to higher order terms which must explain the fitted value $r_* \approx 12.4$ g kg^{-1} observed for usual atmospheric conditions.

5   Conclusions

It has been shown that it is possible to justify mathematically the first order approximation of θ_s derived in M11 and denoted by $(\theta_s)_1 \approx \theta_l \, \exp(\Lambda_r\, q_t)$, which depends on the two Betts' variables (θ_l, q_t) and $\Lambda_r \approx 5.87$, leading to $s \approx s_{ref} + c_{pd}\,\ln(\theta_l) + c_{pd}\,\Lambda_r\, q_t$.

A second order approximation is derived and compared to observed vertical profiles of cumulus and stratocumulus, leading to $s \approx s_{ref} + c_{pd}\,\ln(\theta_l) + c_{pd}\,\Lambda_*\, q_t$, where the second order term $\Lambda_* = \Lambda_r \, - \, \gamma\,\ln(r_v/r_*)$ depends on the constant $\Lambda_r \approx 5.87$, on the mixing ratio r_v, and on a tuning parameter $r_* \approx 12.4$ g kg^{-1}.

The use of the second order term Λ_* depending on the non-conservative variable $r_v \approx q_t - q_l - q_i$ can explain why it is needed to replace the Betts' potential temperature θ_l for computing flux of moist-air entropy:

$$\overline{w'\theta_s'} \approx \exp(\Lambda_*\, q_t)\,\overline{w'\theta_l'} + \Lambda_*\,\theta_s\,\overline{w'q_t'} - (\gamma\, q_t\,\theta_s/r_v)\,\overline{w'r_v'},$$

the last term depending on $\overline{w'q_t'}$ minus $\overline{w'q_l'}$ or $\overline{w'q_i'}$.

References

• Marquet P. (2011). Definition of a moist entropic potential temperature. Application to FIRE-I data flights. *Q. J. R. Meteorol. Soc.* **137** (656) : p.768–791.

• Marquet P. and Geleyn, J.-F. (2015). Formulations of moist thermodynamics for atmospheric modelling. To appear in *Parameterization of Atmospheric Convection*, Volume II (R. S. Plant and J. I. Yano, Eds.), Imperial College Press, in press.

Definition of Total Energy budget equation in terms of moist-air Enthalpy surface flux

Pascal Marquet

Météo-France. CNRM/GMAP. Toulouse. France. *E-mail: pascal.marquet@meteo.fr*

1 Motivations

The way moist-air surface heat flux should be computed in atmospheric science is still a subject of debate. It is explained in Montgomery (1948, M48), Businger (1982, B82), more recently Ambaum (2010, §3.7), that uncertainty exists concerning the proper formulation of surface heat fluxes, namely the sum of "sensible" and "latent" heat fluxes, and in fact concerning these two fluxes if they are considered as separate fluxes.

It is shown in M48 that eddy flux of moist-air energy must be defined as the eddy transfer of moist-air specific enthalpy $h = e_{int} + p/\rho = e_{int} + R\,T$, where e_{int} is the internal energy. However, the way the moist-air specific enthalpy h is computed in M48 still depends on some arbitrary assumptions concerning reference value of dry-air or water-vapour enthalpies, which are set in M48 to arbitrary conventional values at a finite reference temperatures different from 0 K.

Consequences of these arbitrary assumptions are studied at length in B82, though without succeeding in computing the moist-air enthalpy in an absolute way.

Issues addressed in M48 and B82 can be overcome by using the specific thermal enthalpies derived in Marquet (2015, M15) for N_2, O_2 and H_2O, namely for the main components of moist air.

In this article this approach is taken to show that Third-law based values of moist-air enthalpy fluxes is the sum of two terms. These two terms are similar to what is called "sensible" and "latent" heat fluxes in existing surface energy budget equation, but a new kind of "latent heat" is emerging in the definition of the moist-air enthalpy flux. Some impacts of this new "latent heat" flux are described in this brief version of a paper to be submitted to the QJRMS.

2 The energy budget equation

Only three kinds of specific energies can be defined in atmosphere if nuclear or chemical reactions are not considered: i) the kinetic energy $e_k = (u^2 + v^2 + w^2)/2$; ii) the potential energy $\phi = g\,z$; iii) the moist-air thermal internal energy $e_{int} = h - p/\rho$ or enthalpy $h = e_{int} + p/\rho$ which are both associated with the First-Law of Thermodynamics.

The total energy equation of a unit mass of moist air is computed for the sum $e_{tot} = e_k + \phi + e_{int}$ by adding the three local equations for e_k, ϕ and e_{int}, yielding

$$\frac{\partial}{\partial t}\left[\,\rho\,(\,e_{int} + \phi + e_k\,)\,\right] = -\boldsymbol{\nabla}.\left[\,\rho\,(\,h + \phi + e_k\,)\,\mathbf{U}\,\right] + \rho\,\dot{q},$$

where $\dot{q}$ is a notation for impacts of radiation and other local sinks and sources of energy. The specific enthalpy h appears in the divergence term because the sum of $-\,\mathbf{U}.\boldsymbol{\nabla}(p)$ and $-p\,\boldsymbol{\nabla}.\mathbf{U}$ in equations for e_k and e_{int}, respectively, is equal to $-\boldsymbol{\nabla}.(\,p\,\mathbf{U}) = -\boldsymbol{\nabla}.[\,\rho\,(p/\rho)\,\mathbf{U}]$, thus leading to the local definition $e_{int} + p/\rho \equiv h$.
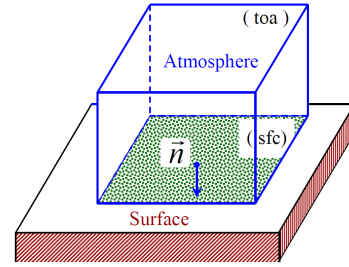

Figure 1: *A column of atmosphere above Earth's surface.*

The total energy budget equation is then computed by integrating this local equation over an infinite vertical column of atmosphere (see Fig.1), leading to

$$\frac{\partial E_{tot}}{\partial t} \;=\; \langle\,\rho\,(\,h + \phi + e_k\,)\,w\,\rangle \;+\; \dot{Q},$$

where lateral fluxes have been neglected. The term $\langle(...)\rangle$ denotes the surface average of $\rho\,(h + \phi + e_k)\,w$, and the integral of "$\rho\,\dot{q}$" is written as $\dot{Q}$.

The exchange of total energy between the column and the surface thus depends on $\langle\,\rho\,(h + \phi)\,w\,\rangle$ which can be rewritten by using Reynolds average $\overline{(...)}$ and perturbation $(...)'$ terms, leading to the local turbulent fluxes of specific enthalpy and potential energy

$$F_h \;\equiv\; \overline{(\rho\,w)'\,h'} \;\approx\; \overline{\rho}\,\,\overline{w'\,h'}\,, \tag{1}$$

$$F_\phi \;\equiv\; \overline{(\rho\,w)'\,\phi'} \;\approx\; \overline{\rho}\,\,\overline{w'\,\phi'}\,. \tag{2}$$

Conclusions are the same as in M48 or B42: from (1), it is needed to know specific values of moist-air thermal enthalpy h, in order to compute $\overline{w'\,h'}$.

3 The specific thermal enthalpy

The moist-air enthalpy is equal to the weighted average of individual (perfect gas) values for dry air, water vapour, liquid water and ice species, leading to $h = q_d\,h_d + q_v\,h_v + q_l\,h_l + q_i\,h_i$. This sum can be computed

according to M15 (with different algebra), leading to

$$h = h_{\text{ref}} + c_{pd}\, T + L_h\, q_t - L_{\text{vap}}\, q_l - L_{\text{sub}}\, q_i \,, \quad (3)$$

where $L_{\text{sub}}(T) \equiv h_v(T) - h_i(T)$,

$$L_h(T) \equiv h_v(T) - h_d(T)\,,$$
$$L_{\text{vap}}(T) \equiv h_v(T) - h_l(T)\,,$$

where $q_t = q_v + q_l + q_i$ is the total water content. The atent heats are in fact "differences in enthalpies". They only depends on temperature and on some reference values, with for instance $L_h(T) = L_h(T_r) + (c_{pv} - c_{pd})\,(T - T_r)$ and $L_h(T_r) = (h_v)_r - (h_d)_r$.

Issues reported in M48 an B82 can thus be understood by a need to know $(h_d)_r$ and $(h_v)_r$ in order to compute $L_h(T_r)$, then $L_h(T)$, and finally "h" via (3). Dry-air and water-vapour reference thermal enthalpies are computed in M15 at 0 C: $(h_d)_r \approx 530$ kJ kg^{-1} and $(h_v)_r \approx 3133$ kJ kg^{-1}. The moist-air reference enthalpy is thus equal to $h_{\text{ref}} = (h_d)_r - c_{pd}\,T_r \approx 256$ kJ kg^{-1}. It is a true constant (whatever T_r may be in atmospheric range of T with constant c_{pd}) and it does not impact on gradient or flux computations.
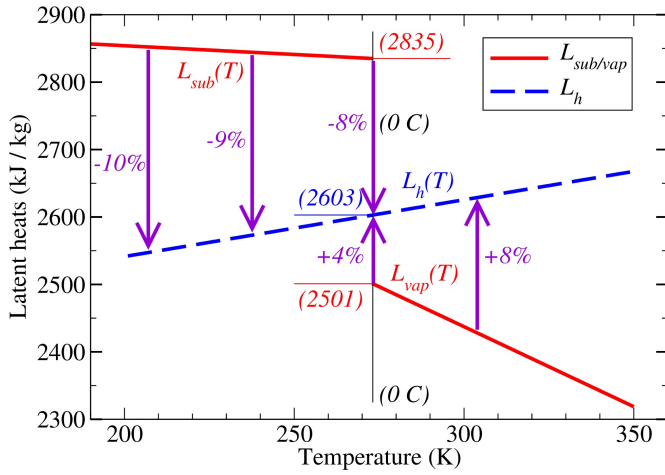

Figure 2: *Comparison of $L_h(T)$ with $L_{\text{vap}}(T)$ and $L_{\text{sub}}(T)$. Unit are in kJ kg^{-1} for latent heats, in K for T.*

Changes of L_{sub}, L_h and L_{vap} with absolute temperature are compared in Fig.2. The dashed straight line represents $L_h(T)$. It is continuous at 0 C and is in between solid lines representing $L_{\text{sub}}(T)$ and $L_{\text{vap}}(T)$.

4 The moist-air enthalpy flux

The moist-air thermal enthalpy fluxes $F_h \approx \overline{\rho}\ \overline{w'\,h'}$ can be computed with h defined by (3), yielding

$$F_h = c_p\, F_T + L_h\, F_v$$
$$+ (L_h - L_{\text{vap}})\, F_l - (L_{\text{sub}} - L_h)\, F_i\,, \quad (4)$$

where moist value of c_p is considered and where $F_T \approx \overline{\rho}\ \overline{w'\,T'}$, $F_v \approx \overline{\rho}\ \overline{w'\,q_v'}$, $F_l \approx \overline{\rho}\ \overline{w'\,q_l'}$ and $F_i \approx \overline{\rho}\ \overline{w'\,q_i'}$ are turbulent fluxes of temperature and water species.

Clearly, $L_h - L_{\text{vap}}$ and $L_{\text{sub}} - L_h$ represent about 4 to 8 % of L_{vap}, and about -8 to -10 % of L_{sub}. The second line of (4) can thus be neglected with an accuracy better than 10 % and $F_h \approx c_p\, F_T + L_h\, F_v$.

However, if liquid water of ice contents exist, it is easy to avoid any approximation by taking into account the second line and the small terms depending on F_l or F_i.

5 Numerical evaluations

From Fig.2 and for Earth's surface temperatures from 0 to 30 C, L_h is about 6 % larger than L_{vap} in average. The change of $L_{\text{vap}}(T)$ by $L_h(T)$ should thus lead to an increase of about 6 % for existing surface latent heat fluxes which are about 100 W m^{-2} in average. Impact of using $L_h(T)$ on global energy budget of atmosphere should thus be of the order of $+6$ W m^{-2} in average. But impact larger than $+50$ W m^{-2} could exist locally.

These values have been confirmed by using short-range forecasts of ARPEGE NWP model, and in particular for convective or frontal regions.

6 Conclusions

It has been shown that computations of budget of total energy imply computations of turbulent fluxes of specific enthalpy, and that it is possible to achieve the program started in M48 and B82 by computing these turbulent fluxes of enthalpy (4) by using reference values of enthalpies derived in M15.

The surface enthalpy flux (4) may replace what are commonly called "latent" and "sensible" heat fluxes, with the use of a new "latent heat" $L_h(T)$ which is the difference in enthalpies of dry air and water vapour. Impacts of using $L_h(T)$ is of the order of $+6$ W m^{-2} in average, and more than $+50$ W m^{-2} locally.

$L_h(T)$ represents physical processes like evaporations over oceans where water vapour enters atmospheric parcels of moist air, this meaning a decrease in q_d at the expense of an increase of q_v, in other words a replacement of dry air by water vapour.

A striking feature imposed by the definition of the moist-air enthalpy (3) is that $L_h(T)$ is continuous at 0 C. This is in direct contradiction to the usual definitions of latent heat fluxes, assumed to be equal to $L_{\text{vap}}\, F_v$ over liquid water and $L_{\text{sub}}\, F_v$ over ice.

References

• M. H. P. Ambaum (2010). *Thermal physics of the atmosphere.* Advancing weather and climate science. Wiley-Blackwell. John Wiley and sons. Chichester.

• J. A. Businger (1982). The fluxes of specific enthalpy, sensible heat and latent heat near the Earth's surface. *J. Atmos. Sci.* **39** (8): p.1889–1892.

• P. Marquet (2015). On the computation of moist-air specific thermal enthalpy. *Q. J. R. Meteorol. Soc.* **141** (686): p.67–84.

• R. B. Montgomery (1948). Vertical eddy flux of heat in the atmosphere. *J. Meteorol.* **5**, (6): p.265–274.

A moist "available enthalpy" norm: definition and comparison with existing "energy" norms

by **Pascal Marquet and Jean-François Mahfouf**
Météo-France. CNRM/GMAP. Toulouse. France.
E-mail: pascal.marquet@meteo.fr

1 Motivation

Several inner-products, based on energy norms, have been used in preliminary 4-D variational assimilation to minimize cost functions. It was supposed that the energy corresponding to observational errors could be distributed equally amongst these different basic prognostic fields.

Inner-products based on the same energy norms are also used to define the (dry) semi-implicit operators and the (dry) normal modes of GCMs or NWP models, as far as they are invariant by the linear set of primitive equations. The same inner-products are currently used for computing dry or moist singular vectors and for determining forecast errors or sensitivity to observations based on tangent linear and adjoint models.

However, it is shown in a paper to be submitted (Marquet and Mahfouf, QJRMS) that these norms suffer from a lack of reliability, since their definitions are not unique and because these "Total Energy Norms" are not based on an "Energy" concept.

This can be illustrated by considering the sum of temperature and water vapour contributions of the total energy norm defined in Ehrendorfer *et al.* (1999, E99) in terms of the quadratic perturbations $(T')^2/2$ and $(q'_v)^2/2$, leading to

$$N_{\text{E99}} \;=\; \frac{c_{pd}}{T_r}\,\frac{\overline{(T')^2}}{2} \;+\; \epsilon(z)\,\frac{(L_{\text{vap}})^2}{c_{pd}\,T_r}\,\frac{\overline{(q'_v)^2}}{2}\;. \quad (1)$$

The first term (temperature contribution) cannot be derived from the enthalpy which roughly varies as $c_{pd}T$ and is linear in temperature. In fact the formulation retained in (1) is based on the Available Potential Energy (APE) of Lorenz, provided that the reference temperature is a constant value T_r. What is usually called "Total Energy Norm" should thus be called "Total APE Norm".

As for the water-vapour contribution (second term) of the norm (1), it is derived from the temperature contribution with the additional hypothesis that changes of temperature and moisture are related by $c_{pd}T' \approx -L_{\text{vap}}q'_v$, namely by assuming conservation of perturbed moist static energy $(c_{pd}T + L_{\text{vap}}q_v)$ in condensation processes. This assumption is not realistic, in particular in all under-saturated regions. For this reason, an arbitrary factor $\epsilon(z)$ is often introduced, which may vary with altitude, though without clear justification.

An alternative definition for the water-vapour contribution of the norm is suggested in Mahfouf and Bilodeau (2007, MB07) by assuming zero departure (at constant pressure) in the relative humidity defined by $q_v/q_{sw}(T,p)$, this implying $q'_v \approx (\Gamma_q)\,T'$ where $\Gamma_q = (\overline{q_v}/\overline{q_{sw}})\,(\partial\,\overline{q_{sw}}/\partial\,T)$, leading to

$$N_{\text{MB07}} \;=\; \frac{c_{pd}}{T_r}\,\frac{\overline{(T')^2}}{2} \;+\; \frac{c_{pd}}{T_r}\,\frac{1}{(\Gamma_q)^2}\,\frac{\overline{(q'_v)^2}}{2}\;. \quad (2)$$

This definition in terms of Γ_q is also arbitrary and may not be valid everywhere.

2 The available enthalpy norm

The dry-air available enthalpy is an Exergy function derived in general thermodynamics. It is defined as $a_h = (h-h_r)-T_r(s-s_r)$ in terms of enthalpy h, entropy s and some reference values $(h_r,\,s_r)$. It is shown in Marquet (1991, 2003) that integral of a_h can replace the APE of Lorenz, leading to a modified temperature contribution of the norm (1) which can be written as

$$N_T = \frac{c_{pd}\,T_r}{(\overline{T})^2}\,\frac{\overline{(T')^2}}{2} = \frac{c_{pd}}{T_r}\left(\frac{T_r}{\overline{T}}\right)^2\,\frac{\overline{(T')^2}}{2} = \frac{\overline{(T')^2}}{V_T}\;, \quad (3)$$

where the variance of temperature is weighted by $V_T = (2\,T_r/c_{pd})\,(\overline{T}/T_r)^2$. The comparison with (1) shows that the additional factor $(T_r/\overline{T})^2$ is not a constant and may vary with pressure or latitude, via the isobaric (or zonal) mean value $\overline{T}(\varphi,p)$.

A moist version of a_h is defined in Marquet (1993, M93) and it is possible to define a "Moist Available Enthalpy Norm". The temperature contribution is still given by (3) and the new water-vapour contribution is expressed in terms of the mixing ratio, leading to

$$N_v \;=\; \frac{R_v\,T_r}{\overline{r_v}}\,\frac{\overline{(r'_v)^2}}{2} \;=\; \frac{\overline{(r'_v)^2}}{V_q}\;, \quad (4)$$

where the variance of water is weighted by $V_q = (2\,\overline{r_v})/(R_v\,T_r)$. Differently from the constant weighting factor in (1), but similarly to the varying one in (2), V_q must clearly decrease with height due to the isobaric (or zonal) mean value $\overline{r_v}(\varphi,p)$.

3 A numerical study

The datasets from MB07 have been used for comparing the quantities $\sqrt{V_T}$ and $\sqrt{V_q}$ estimated from the definition of moist "energy" norms (E99, MB07) and present Exergy (Available Enthalpy) norm against standard deviation of analysis increments (S_T, S_q) derived in MB07 from the CMC 3DVAR system.
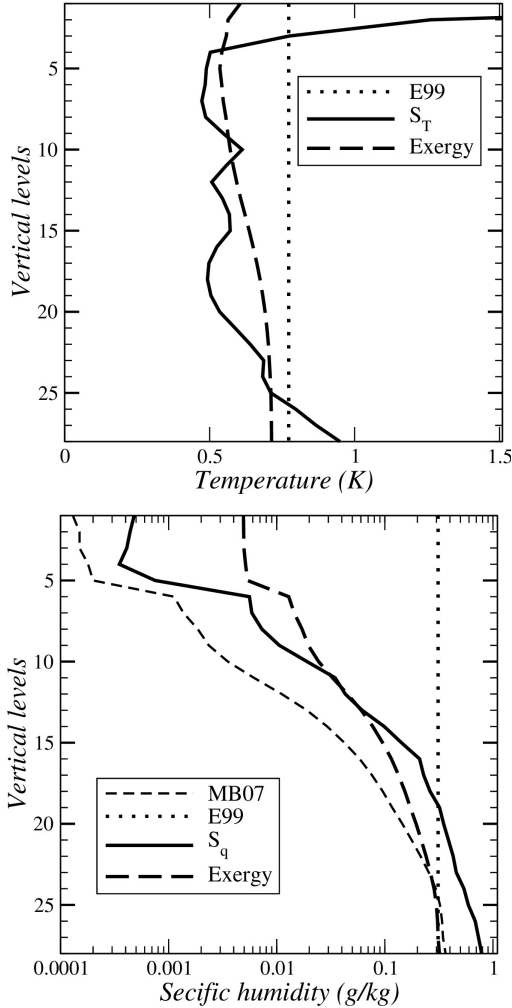

Figure 1: *Comparison of quantities $\sqrt{V}$ estimated from the definition of moist norms against standard deviation of analysis increments S_T and S_q.*

It is shown in Fig.1 (upper panel) that the Exergy norm (3) generating a term $\sqrt{V_T}$ (heavy dashed) varies with height and is in better agreement with S_T (solid) than the constant E99 value (dotted), in particular within the troposphere (below level 5).

Similarly, it is shown in Fig.1 (lower panel) that the Exergy norm (4) generates a term $\sqrt{V_q}$ (heavy dashed) which varies with height and is in much better agreement with S_q (solid) than the constant E99 value (dotted). The norm (2) defined in MB07 is plotted as thin dashed line and is in better agreement with S_q, in particular in the stratosphere above level 5.

4 Conclusions

It has been shown that it is possible to define a moist-air norm based on the concept of "Available Enthalpy" (or "Availability function" or "Exergy").

This new Exergy norm is in close agreement with standard deviation of analysis increments, and a water-vapour contribution is obtained, without the need of unclear and arbitrary assumptions.

The improvement observed with the use of $\sqrt{V_T}$ in the temperature contribution of the norm (3) is a pleasant surprise. As for the water contribution of the norm (4), the use of $\sqrt{V_q}$ can explain the observed strong decrease of the norm with height by about two order of magnitude, and this result is obtained without arbitrary assumptions or use of $\epsilon(z)$.

A striking feature is that liquid water or ice cloud contents do not contribute to an independent quadratic norm depending on $(r'_l)^2$ or $(r'_i)^2$. Only $(r'_v)^2$ must be considered, with q_l and q_i only impacting the moist definition of c_p in factor of the temperature contribution of the norm, with small impacts on the norm itself.

Moreover, the surface pressure contribution which is included in all norm definitions also results from the Available Enthalpy norm (not shown), leading to a complete explanation of all three temperature, surface pressure and water vapour contributions of the new moist-air norm.

The above results justify the proposed method, that is to start with an availability function (which generalizes the APE of Lorenz to the case of a moist atmosphere) in order to build a physically sound moist norm.

References

● Mahfouf, J.-F., Bilodeau, B. (2007). Adjoint sensitivity of surface precipitation to initial conditions. *Mon. Wea. Rev.* **135**: p.2879–2896.

● Ehrendorfer, M., Errico, R. M and Reader, K., D. (1999). Singular-Vector perturbation growth in a primitive equation model with moist physics. *J. Atmos. Sci.* **56**: p.1627–1648.

● Marquet P. (1991). On the concept of exergy and available enthalpy: application to atmospheric energetics. *Q. J. R. Meteorol. Soc.* **117**: p.449–475.

● Marquet P. (1993). Exergy in meteorology: definition and properties of moist available enthalpy. *Q. J. R. Meteorol. Soc.* **119**: p.567–590.

● Marquet, P. (2003). The available-enthalpy cycle. I: Introduction and basic equations. *Q. J. R. Meteorol. Soc.* **129**: p.2445–2466.

Application of delta-four-stream approximation to the JMA-GSM shortwave radiation scheme: preliminary results

Ryohei Sekiguchi
Climate Prediction Division, Japan Meteorological Agency, Tokyo, Japan
E-mail: r_sekiguchi@met.kishou.go.jp

1. Introduction

The current operational shortwave radiation (SW) scheme implemented in the Japan Meteorological Agency Global Spectral Model (JMA-GSM, Yonehara et al. 2014) uses the delta-Eddington two-stream approximation method for the computation of radiative transfer with absorption and multiple scattering processes. This method is computationally efficient under clear-sky and cloudy-sky conditions, and is widely used in SW schemes for global models. However, as the two-stream approximation may cause large computational errors in the calculation of shortwave flux and the heating rate under cloudy-sky conditions, there is a need for higher-order approximation in the model's SW scheme. Against such a background, a delta-four-stream approximation method was tested with the JMA-GSM SW scheme. In this study, the delta-four-stream discrete ordinate method (Liou et al. 1988; Zhang et al. 2013) was applied as an alternative to the currently used delta-Eddington approximation method.

2. Experiment configuration

The accuracy of the delta-four-stream approximation method was investigated using a single column model (SCM). The current SW scheme was used in the control experiment (CNTL), and the delta-four-stream discrete ordinate method was used in the test experiment (TEST). The results of both experiments were compared with the delta-32-stream discrete ordinate method (Stamnes et al. 1988) as a benchmark.

Mid-latitude summer standard atmosphere was chosen to represent a typical vertical profile for temperature, humidity and ozone as given in the SCM. Clear-sky case, low-cloud case with thick cloud lying around 850-hPa height, and high-cloud case with thin cloud lying around 250-hPa height were considered. The surface albedo and the cosine of the solar zenith angle were set to 0.2 and 0.8, respectively. The effects of aerosols were neglected for simplicity.

3. Verification of the delta-four-stream approximation method

Tables 1 and 2 show the results of the SCM experiments for shortwave fluxes. Compared with the corresponding benchmark results in the high-cloud case, CNTL shows negative errors up to 5 W/m^2 for downward flux at the surface and positive errors up to 7 W/m^2 for upward flux at the top of the atmosphere. This suggests that reflection tends to be overestimated with the current SW scheme in this case. The application of delta-four-stream approximation is expected to improve the accuracy of calculation for multiple scattering processes, especially in the optically thin case where the scattering field differs significantly from the two-stream assumption. The shortwave flux errors seen in CNTL were reduced as expected in TEST to less than 0.5 W/m^2.

In the low-cloud case, the accuracy of shortwave fluxes calculated in CNTL was comparable to that of TEST, but a large difference in the shortwave heating rate was observed. This error as compared to the benchmark results is shown in the panel on the right of Figure 1. CNTL (shown by the blue line) exhibits negative shortwave heating error at the cloud top and positive error at the cloud base; notably, the error at the cloud top exceeds 0.9 K/day. It is possible that absorption due to cloud is underestimated with the current SW scheme, meaning that shortwave flux absorption in the upper part of the cloud layer weakens and the energy that should be absorbed there reaches the lower part of the cloud layer. These errors are also reduced by the application of the delta-four-stream method (TEST, red line) to about 0.1 K/day.

Accuracy improvement for shortwave flux and the heating rate was also observed with other atmospheric profiles and solar zenith angles (not shown).

4. Summary and future plans

In this study, the delta-four-stream approximation method was tested in the JMA-GSM SW scheme and its accuracy was investigated. Idealized SCM experiments showed that the delta-four-stream approximation method reduces the

shortwave flux and heating rate errors observed with the operational delta-Eddington approximation method, especially in cloudy-sky conditions. The results presented here are preliminary; the impact of this method on the operational JMA-GSM will be investigated as the next step. For operational use, the computational efficiency of the scheme should also be evaluated.

Table 1: Calculated downward shortwave flux at the surface in the SCM (unit: W/m^2). CNTL, TEST, and benchmark represent each experiment. Differences of CNTL and TEST results from the benchmark are also shown.

	benchmark	CNTL	CNTL − benchmark	TEST	TEST − benchmark
clear-sky	841.09	838.53	−2.56	841.56	+0.47
low-cloud	168.98	168.56	−0.42	169.39	+0.41
high-cloud	820.66	815.02	−5.64	820.69	+0.03

Table 2: As per Table 1, but for upward shortwave flux at the top of the atmosphere.

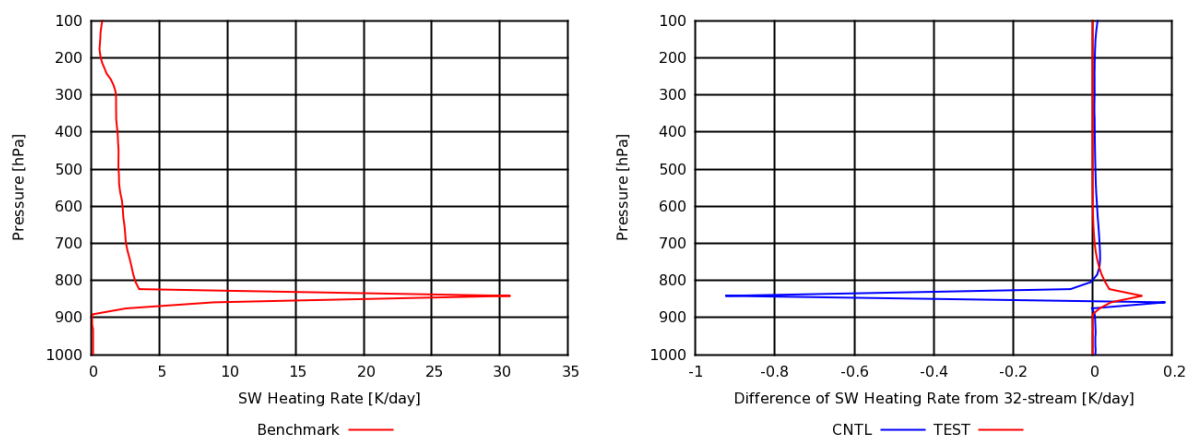|	benchmark	CNTL	CNTL − benchmark	TEST	TEST − benchmark
clear-sky	190.20	192.79	+2.59	189.83	−0.37
low-cloud	653.88	654.60	+0.72	652.64	−1.24
high-cloud	204.04	211.18	+7.14	203.59	−0.45

Figure 1: Calculated shortwave heating rate profile in the SCM (unit: K/day). Left: benchmark results; right: differences in CNTL (blue line) and TEST (red line) from the benchmark

References

Liou, K.-N., Q. Fu, and T. P. Ackerman, 1988: A simple formulation of the delta-four-stream approximation for radiative transfer parameterizations. *J. Atmos. Sci.,* **45**, 1940–1947.

Stamnes, K., S. C. Tsay, W. J. Wiscombe, and K. Jayaweera, 1988: Numerically stable algorithm for discrete ordinate method radiative transfer in multiple scattering and emitting layered media. *Appl. Opt.*, **27**, 2502–2509.

Yonehara, H., M. Ujiie, T. Kanehama, R. Sekiguchi, and Y. Hayashi, 2014: Upgrade of JMA's Operational NWP Global Model. *CAS/JSC WGNE Res. Activ. Atmos. Oceanic. Modell.*, **44**, 06.19–06.20.

Zhang, F., Z. Shen, J. Li, X. Zhou, and L. Ma, 2013: Analytical delta-four-stream doubling-adding method for radiative transfer parameterizations. *J. Atmos. Sci.*, **70**, 794–808.

Improving 2-m Temperature Forecasts in the NCEP Global Forecast System

Weizhong Zheng[1,2], Michael Ek[1], Helin Wei[1,2] and Jesse Meng[1,2]

[1]*NOAA/NCEP/Environmental Modeling Center, College Park, MD 20740, USA*
[2]*IMSG at NOAA/NCEP/Environmental Modeling Center, College Park, MD 20740, USA*
Email: Weizhong.Zheng@noaa.gov

Like precipitation, the accurate prediction of 2-m temperature is one of the essential components for numerical weather prediction, and is also considered a challenging task because of the multiplicity of physical processes and their complex interactions (Holtslag et al., 2013, Steeneveld, 2014). It has long been known that the NCEP Global Forecast System (GFS) has large errors in the forecast of near-surface temperature for some seasons. In particular, large biases in late afternoon and nighttime 2-m temperatures usually happen in the spring, autumn and winter seasons. This study focuses on improving near-surface air temperature forecasts under stable conditions in the GFS model. We identify the systematic deficiencies and cause of errors in near-surface temperature forecasts by investigating the physics of the Noah land surface model and land-atmosphere interactions, and find a practical solution to reduce these kinds of forecasting errors. The modifications were proposed to include updated roughness length and preventing the coupled system from decoupling. Sensitivity tests for case studies and two one-month experiments for the summer and winter seasons were performed. The results demonstrate a substantial reduction of errors in near-surface 2-m air temperature forecasts using the proposed modifications, and include a notable reduction in bias and root-mean-square error of temperature in the lower atmosphere. Furthermore, surface dew point temperature, surface wind speed and scores for light and medium precipitation are also improved.

Figure 1 shows a winter case over snowpack with the proposed modifications in the GFS. The sensitivity test (EXP) demonstrates that the large cold bias of 2-m temperature occurring over New York State was reduced in the experiment. At Utica, New York, the 2-m temperature for the control run (CTL) dropped quickly between 21Z, Feb. 16 and 00Z, Feb. 17, 2015 and the rapid cooling was up to 15 °C during these 3 hours, indicating an unrealistic decoupling of the atmosphere from the surface. Compared to the observations, the sensitivity test substantially avoided rapidly dropping the temperatures. This decoupling phenomenon happened again on the following day, and the sensitivity test again prevented it.

The one-month GFS free forecasts for the winter season show good improvement in 2-m temperature over the CONUS regions. Figure 2 gives 2-m temperature and its root-mean-square error (RMSE) averaged over the northwest CONUS. The sensitivity test reduced the cold bias in late afternoon and early evening up to 1.2 °C, with RMSE reduced up to 1 °C which was about 25% of the total error.

References

Holtslag, A. A. M., Svensson, G., Baas, P., Basu, S., Beare, B., Beljaars, A. C. M., et al. (2013). Stable atmospheric boundary layers and diurnal cycles: challenges for weather and climate models. Bull. Am. Meteorol. Soc. 94, 1691–1706. doi: 10.1175/BAMS-D-11-00187.1

Steeneveld, Gert-Jan, (2014). Current challenges in understanding and forecasting stable boundary layers over land and ice. *Frontiers in Environmental Science* 2, 41.
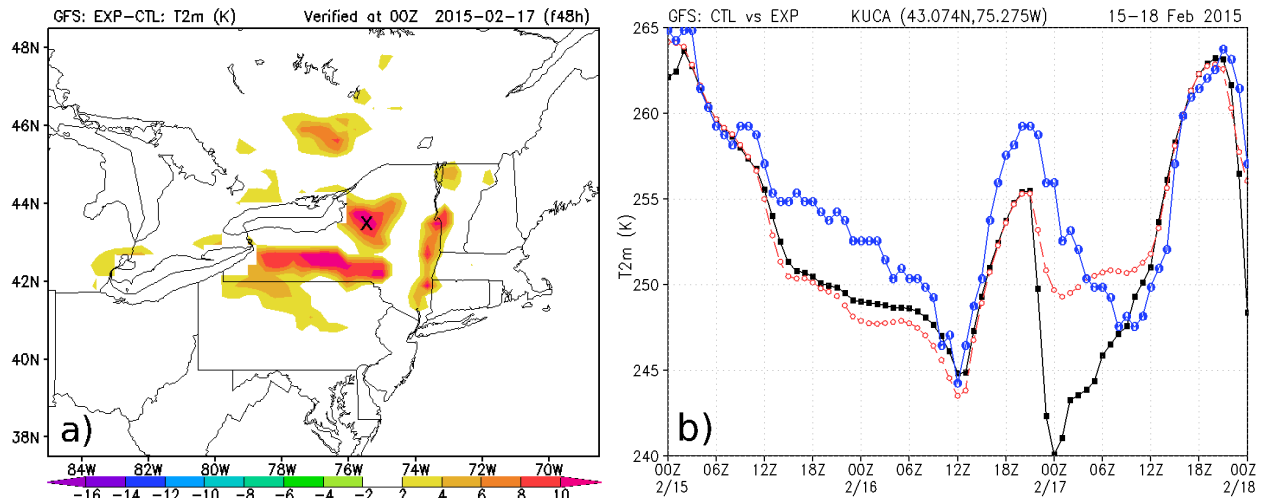

Fig.1 Difference of 2-m temperature between EXP and CTL at 00Z, Feb.17, 2015 (a); and (b) 2-m temperature time series at Utica labeled with "X" in (a) for observation (blue line), CTL (black line) and EXP (red line).
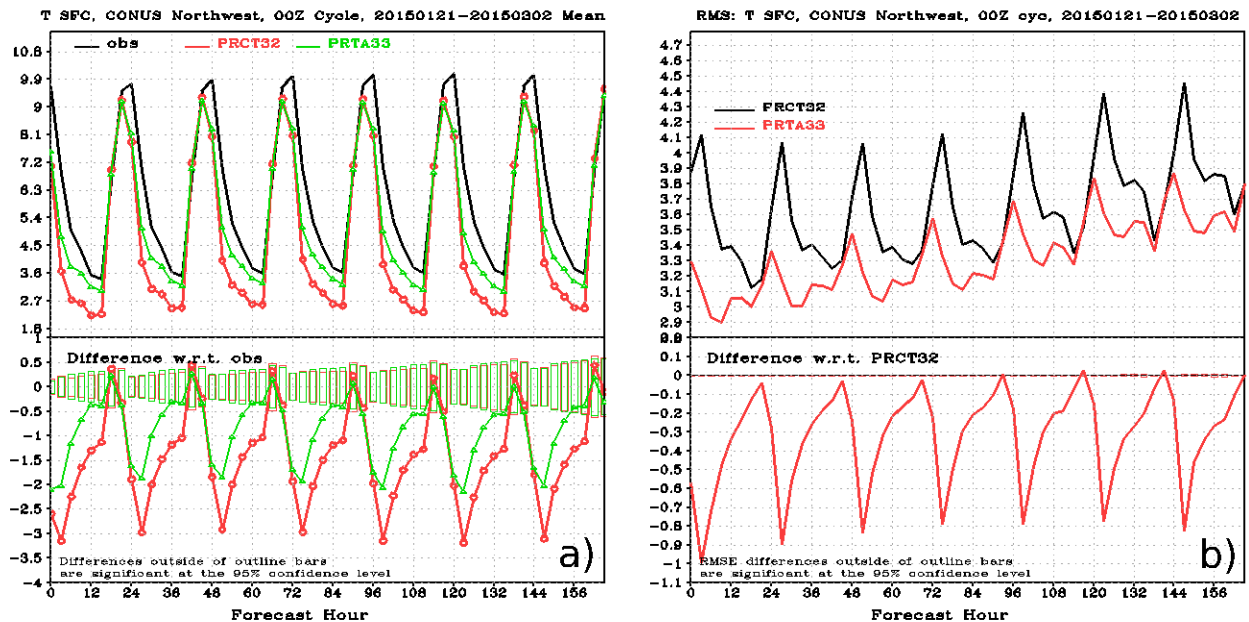

Fig. 2 Comparison of 2-m temperatures for GFS tests averaged over a period from Jan. 21 to March 2, 2015 over the northwest CONUS. (a) 2-m temperatures for the observations (black line), CTL (red lines) and EXP (green lines); (b) RMSE for CTL (black line) and EXP (red line), and their difference.